RSC Advances

PAPER

View Article Online
View Journal | View Issue

Cite this: *RSC Adv.*, 2026, **16**, 11543

Clinical potential for infected wound care: synergistic photothermal-photodynamic therapy using a conjugation-bridge modulated D–A–D porous organic polymer

Jie Zheng,[a] Lei Ju,[a] Jie Sun,[c] Linlin Xu[a] and Junshan Zhang *[b]

Porphyrin-based photosensitizers (PSs) often suffer from aggregation-caused quenching (ACQ) due to strong π–π stacking, which severely compromises their therapeutic activity. To address this, we leverage the inherently rigid and distorted frameworks of porous organic polymers (POPs) to physically impede such detrimental stacking, thereby preserving the photoactivity of the embedded porphyrin units. By employing a conjugation-bridge engineering strategy, we synthesized a series of porphyrin-based conjugated microporous polymers (CMPs). Among them, the optimal material, TPA-POR, is constructed from an electron-donating TPA unit, specifically, 1,1′,1″-(nitrilotris(benzene-4,1-diyl))tris(ethan-1-one) and electron-accepting triazine nodes, denoted as 6,6′,6″,6‴-(porphyrin-5,10,15,20-tetrayltetrakis(benzene-4,1-diyl))tetrakis(1,3,5-triazine-2,4-diamine). In this architecture, the porphyrin components serve as the electron-donor cores linked to the triazine units, consistent with their well-known role as PSs. This molecular design gives TPA-POR a distinct donor–acceptor–donor (D–A–D) topology. This rational design confers multiple integrated advantages that synergistically address the key challenges in phototherapy. The inherently positive charge of the structure allows for precise electrostatic targeting to bacterial surfaces, which not only concentrates the therapeutic agent but also critically shortens the diffusion path for short-lived ROS, maximizing their localized impact. TPA-POR exerts its antibacterial effect through dual photodynamic pathways. Its Type I mechanism efficiently generates ROS, such as hydroxyl radicals (•OH), enabling effective therapy even in hypoxic microenvironments. Concurrently, the Type II pathway provides complementary activity under oxygen-replete conditions. This dual capability reduces reliance on ambient oxygen, overcoming a key limitation of conventional photodynamic therapy. Furthermore, these photodynamic actions are synergized by the material's intrinsic photothermal properties and its rigid, nanostructured surface, which promotes physical interaction with bacteria. Together, these integrated mechanisms ensure potent and reliable efficacy across diverse oxygen tensions. Consequently, TPA-POR exhibits potent antimicrobial activity, achieving near-complete inactivation of both *S. aureus* and *E. coli* at a low concentration of 300 μg mL^{-1} and effectively promoting the healing of infected wounds *in vivo*. This work demonstrates a multifaceted design that integrates the anti-quenching scaffold of POPs with a functional D–A–D architecture to overcome key limitations in photodynamic therapy.

Received 16th December 2025
Accepted 11th February 2026

DOI: 10.1039/d5ra09715k

rsc.li/rsc-advances

Introduction

Bacterial infections, recognized as a leading pathogenic threat, present a major global challenge by driving a wide spectrum of diseases that endanger public health and impede socioeconomic development.[1–3] This crisis is further intensified by the declining effectiveness of conventional antibiotics,[4] making the pursuit of antibiotic-free sterilization methods an urgent priority.[5] Among these, photo-inactivation (PI) has emerged as a highly promising strategy, valued for its high efficiency, broad-spectrum activity, and non-invasive nature.[6] The success of PI fundamentally depends on the performance of photosensitizers (PSs), which mediate the conversion of light energy into cytotoxic reactive oxygen species (ROS) or localized heat.[7]

Over decades of development, diverse PSs have been explored, broadly classified into organic materials (porphyrins, phenothiazinium dyes, and phthalocyanines) and inorganic counterparts, including carbon dots, metal oxides, and noble

[a]*Department of Midwifery, Weifang Nursing Vocational College, Weifang 261041, China*

[b]*Weifang People's Hospital, Shandong Second Medical University, Weifang, 261041, Shandong, PR China. E-mail: zhangjunshan_1@163.com*

[c]*Computer and Mathematics Teaching & Research Section, Weifang Nursing Vocational College, Weifang 261041, Shandong, PR China*

metal nanoparticles.[8–10] While inorganic PSs often face challenges related to long-term biocompatibility, organic PSs offer superior structural tunability and biodegradability.[11,12] However, the practical application of organic PSs, especially in antibacterial contexts, is hindered by several interrelated limitations. Porphyrin derivatives, in particular, suffer from a strong tendency for π–π stacking and self-aggregation, which quenches their photoexcited states and drastically diminishes photodynamic activity.[13,14] This not only lowers ROS yields but also creates a spatial barrier that restricts their action. Moreover, even when aggregation is mitigated, the inherently short diffusion radius and rapid decay of photogenerated ROS, such as singlet oxygen, require close proximity to bacterial targets for effective lethality.[15] Compounding these spatial constraints, the dominant Type II photodynamic pathway relies heavily on local oxygen concentration, which is often severely depleted in biofilm-associated and deep-tissue infections, imposing a critical environmental limitation on therapeutic efficacy.[16]

To address these challenges, the design of multifunctional nanoplatforms capable of simultaneously targeting bacterial infection, oxidative stress, and the hypoxic wound microenvironment represents a promising direction. Recent advances include intelligent ZIF-based systems that combine photothermal and chemodynamic therapy with oxygen evolution properties, demonstrating significant potential in infected wound healing.[17] Another promising approach involves constructing solid-state PSs within rigid, porous frameworks. By immobilizing photoactive units in a distorted polymer network, aggregation can be physically suppressed.[11] The three-dimensional architecture of porous organic polymers (POPs) prevents close π–π stacking, thereby preserving and even enhancing the photoactivity of embedded chromophores.[12] This solid-state, nanostructured design also facilitates engineered interactions at the material–bacteria interface. A contorted backbone can create a microscopically rough and abrasive surface topology, potentially enhancing physical disruption of bacterial membranes.[18] Furthermore, high porosity supports mass transfer and improves oxygen diffusion, which is essential for efficient ROS generation.[13,14]

Among various porous scaffolds, conjugated microporous polymers (CMPs) have gained prominence as robust platforms for heterogeneous photosensitizers. Characterized by extended π-conjugation, tunable pore architectures, high surface areas, and excellent physicochemical stability, CMPs are well-suited for antimicrobial phototherapy.[15] Importantly, their molecular structure can be precisely tailored at the monomer level, enabling the rational design of donor–acceptor (D–A) systems to improve charge separation for enhanced ROS yields, as well as the incorporation of functional groups to modulate surface properties.[19]

In this study, we synthesized a series of porphyrin-based CMPs with enhanced photoactivity *via* a one-pot polymerization of a tetraaldehyde-functionalized porphyrin with acetyl-substituted linkers of varying conjugation lengths. The rigid and contorted backbone of these CMPs effectively inhibits porphyrin self-aggregation. The optimal material, TPA-POR, constructed from triphenylamine donor and triazine acceptors in a donor–acceptor–donor (D–A–D) topology, was rationally designed to concurrently address key challenges in antibacterial phototherapy. This architecture delivers several integrated benefits. It promotes intramolecular charge separation for enhanced photodynamic efficiency, inherently suppresses aggregation-caused quenching (ACQ), and carries a permanent positive surface charge that enables strong electrostatic adhesion to negatively charged bacterial membranes. This localization drastically shortens the diffusion path for short-lived ROS, maximizing their bactericidal effect. Critically, TPA-POR operates through both Type I and Type II photodynamic pathways, ensuring sustained ROS generation even under hypoxic conditions typical of infected tissues.[20–22] This work establishes a design pathway toward high-performance solid-state photosensitizers capable of addressing the persistent challenge of antibiotic resistance.

Results and discussions

As shown in Scheme 1, four CMPs were facilely prepared *via* a one-pot solvothermal synthesis, involving a condensation reaction between acetyl and amino functionalities, leading to the formation of a cross-linked network. Briefly, the 5,10,15,20-tetrakis(4-(2,4-diaminotriazinyl)phenyl)porphyrin (Por) was polymerized with either the C3-symmetric 4,4′,4″-triacetyltriphenylamine (TPA) or the C2-symmetric 4,4′-diacetylbiphenyl (BP), 1-(7-acetyl-9*H*-carbazol-2-yl)ethanone (CB) and 1,4-diacetylbenzene (BE) aromatic monomers with different conjugations *via* the simple solvothermal synthesis.[23] The final products were powdery materials, denoted as TPA-POR (brownish black powder), BP-POR (black powder), CB-POR (brown powder) and BE-POR (black powder), respectively. The detail for the synthesis was given in the SI.

The bonding of as-synthesized CMPs was initially investigated *via* the Fourier infrared spectrum (FT-IR, Fig. 1a and S1). As seen, apart from the feature signal of reaction monomers, the FT-IR spectra of the as-prepared CMPs all displayed the characteristic stretching vibration belonging to the C=N bonds located at ~1700 cm^{-1}.[24] Meanwhile, the concurrent disappearance of the acetyl (~1670 cm^{-1}) and amine (~3300 cm^{-1}) demonstrated the successful conversion of the starting materials into the desired extended conjugated products.[25,26] Solid-state cross-polarization magic angle spinning ^{13}C-nuclear magnetic resonance (CP/MAS, ^{13}C-NMR) spectra was performed to further investigate the chemical structure of as-synthesized TPA-POR (Fig. 1b). Noteworthily, TPA-POR presented well-resolved carbon signals ranged from 0 to 200 ppm. The shifts distributed around 15 ppm was assigned to the saturated carbon in the methyl group. And the remaining peaks ranged from 120–150 ppm was attributed to the sp^2 hybridized aromatic carbon in the porous skeletons.[27]

To further confirm the formation of the linkages, we performed XPS analysis (Fig. S2a). The core-level N 1s spectrum can be deconvoluted into two primary component peaks. The dominant peak, located at a binding energy of 398.76 eV, is unambiguously assigned to the imine nitrogen (–C=N–) formed *via* the condensation reaction. This provides direct

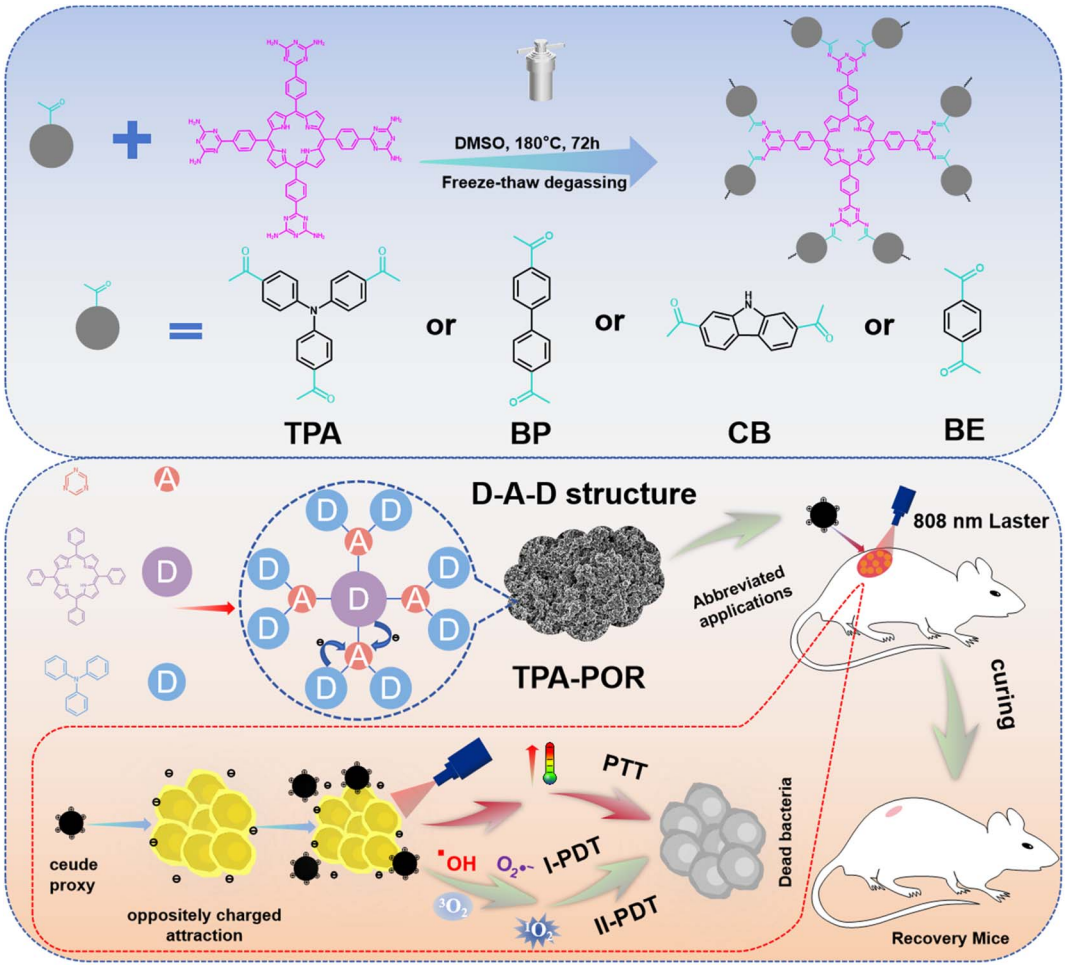

Scheme 1 Schematic diagram of the synthesis and antimicrobial mechanism of TPA-POR.

spectroscopic evidence for the successful formation of the proposed polymer network linkage. A second peak is observed at a higher binding energy of 400.19 eV, which is characteristic of amine-type nitrogen atoms within aromatic C–N environments, originating from the diaminotriazine building units. Taken together, the clarified reaction sites, refined FT-IR deconvolution, as well as direct solid state ^{13}C NMR XPS identification of imine nitrogen offer robust, multi-faceted validation of the proposed condensation pathway and the resulting chemical structure.

The powder X-ray diffraction (XRD) patterns of TPA-POR displayed only a broad peak around 23°, indicating the amorphous nature of the as-synthesized polymers (Fig. S2b). Furthermore, thermogravimetric analysis (TGA) was performed to assess the thermal stability of TPA-POR (Fig. S2c). The data show stability up to 240 °C with a slight mass loss (less than 9%) below 100 °C, due to the loss of water absorbed by the polar, N-rich polymer backbone.[28] The porosity of TPA-POR was determined using low-temperature nitrogen uptake measurements at 77 K. As shown in Fig. 1c, the isotherm of TPA-POR exhibited a vertical increase in the low pressure range ($P/P_0 < 0.01$), followed by a pronounced hysteresis loop, indicating a micro/mesoporous structure.[29] The specific BET surface areas and cumulative total volume of TPA-POR were calculated to be 151.5 $m^2\ g^{-1}$ and 0.086 $cm^3\ g^{-1}$, respectively. Additionally, the pore size distribution (PSD) curve confirmed the coexistence of micropores and mesopores in TPA-POR, with a main peak centered at 5.5 nm and two secondary peaks at 7.97 nm and 36.6 nm. Then, the surface potential (Fig. 1e) and particle size (Fig. 1f) of TPA-POR were respectively explored *via* zeta-potential and dynamic light scattering (DLS). The corresponding results demonstrated the positively charged surface charge of the TPA-POR (+30.06 mV), which could well stick to the negatively charged bacterial surface (−31.33 mV and −15.16 mV for *E. coli* and *S. aureus*). And the surface potential of bacteria was decreased significantly after mixing with TPA-POR.[30] Simultaneously, the particle size analysis revealed the particles were predominantly within the range of 450 to 650 nm.

Scanning electron microscopy (SEM) and transmission electron microscopy (TEM) were then used to observe the morphological features of TPA-POR. As shown in Fig. 2a and b, TPA-POR featured coral-like surface morphology with a branch-like continuous porous skeleton throughout the polymer matrix. Fig. 2c and d showed the TEM of TPA-POR at different scale bars. As observed, TPA-POR exhibits a monolithic structure composed of irregular particles, with interconnected pores

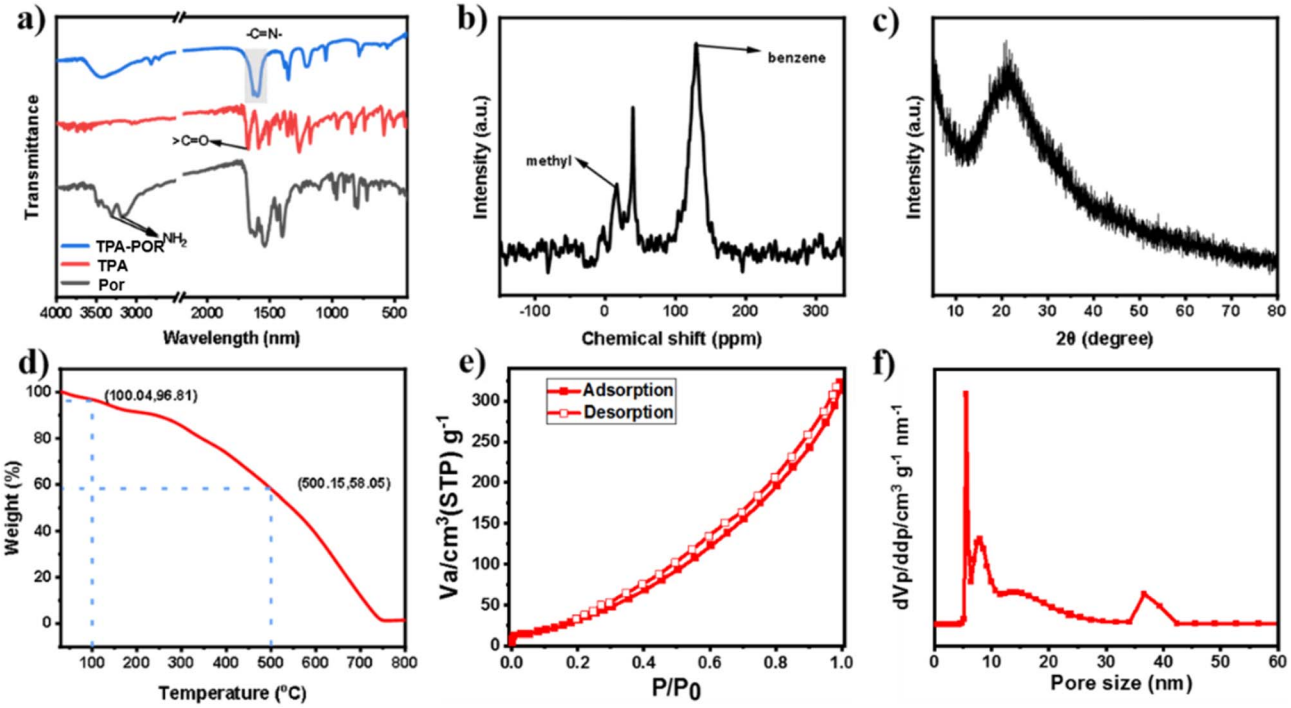

Fig. 1 (a) FT-IR Spectroscopy of Porphyrins, TPA and TPA-POR; (b) solid-state ^{13}C NMR spectra of TPA-POR; (c) low-temperature N_2 uptake isotherm of TPA-POR at 77 K; (d) NLDFT pore width analysis of TPA-POR; (e) surface potential of TPA-POR and bacteria (Group I: TPA-POR, II: *E. coli*, III: *S. aureus*, IV: TPA-POR + *E. coli*, V: TPA-POR + *S. aureus*); (f) particle size distribution of TPA-POR.

widely distributed across the carbon skeleton. Moreover, distinct protrusions along its edges contribute to a rough surface topography, which not only facilitates bacterial attachment but also contributes to the disruption of bacterial structures to some extent. The high-resolution TEM (HR-TEM, Fig. 2e) verified the widely presence of micropore visible from the light and shade contrast. Energy-dispersive spectroscopy (EDS) analysis and the corresponding elemental mapping of TPA-POR (Fig. 2g and S3) confirmed its composition, revealing a carbon-dominated polymer matrix (C, 90.67%) with uniformly distributed nitrogen (N, 7.63%) and oxygen (O, 1.7%). Moreover, transmission electron microscopy (TEM) images of the other three samples (BP-POR, CB-POR, and BE-POR) showed that, similar to TPA-POR, they are also amorphous materials composed of irregularly sized particles (Fig. S4). Thus, the rigid, distorted cationic framework establishes a rough, nanostructured interface with high surface area, which promotes strong bacterial adhesion through localizing the therapeutic agent and enhancing the efficacy of subsequent ROS and heat generation.

The extended conjugated structure of the synthesized polymers prompted us to investigate their photophysical properties. UV-visible-near-infrared (UV-vis-NIR) absorption spectra were collected to evaluate the optical absorption capabilities of the four samples.[31] As shown in Fig. 3a, all samples exhibited broad absorption across 200–900 nm. Among them, TPA-POR displayed the strongest absorption under identical conditions (300 μg mL^{-1}), with absorbance increasing at higher concentrations (Fig. 3b), indicating favorable light-harvesting ability. Given their strong NIR absorption, we further examined the photothermal conversion performance of the polymers (300 μg mL^{-1}) under 808 nm laser irradiation (1.0 W cm^{-2}, 10 min). As illustrated in Fig. 3c, TPA-POR showed the most pronounced temperature rise, increasing rapidly from 27.3 to 69.5 °C, confirming its superior photothermal activity. This result highlights how conjugation-bridge modulation enhances the photothermal properties of the synthesized CMPs. The outstanding performance of TPA-POR can be attributed to its distinct D–A–D topology featuring the TPA donor unit, which likely facilitates more efficient intramolecular charge transfer and stronger light absorption compared to the other bridges (BP, CB, BE). Therefore, TPA-POR was selected as the PS for all subsequent experiments, using pure water as the control. Its photothermal response was evaluated by monitoring temperature increases under 808 nm NIR laser irradiation, with variations in either material dosage or laser power. As shown in Fig. 3d, the temperature of TPA-POR dispersion was remarkably increased with the extension of irradiation time and the sample dose. Furthermore, as verified by the results in Fig. 3e, the photothermal conversion effect of TPA-POR also positively correlated with the NIR laser power densities. All these results demonstrated the photothermal efficiency of TPA-POR could be facilely and precisely controlled by the finely regulation on the sample concentration, illumination time, and the laser power density. The temperature increment of the aqueous dispersion solution of TPA-POR varied from 19.8 °C to 60.4 °C with the increase of concentration (0–400 μg mL^{-1}) after 10 min of NIR irradiation (1.0 W cm^{-2}). And the warming process of TPA-POR

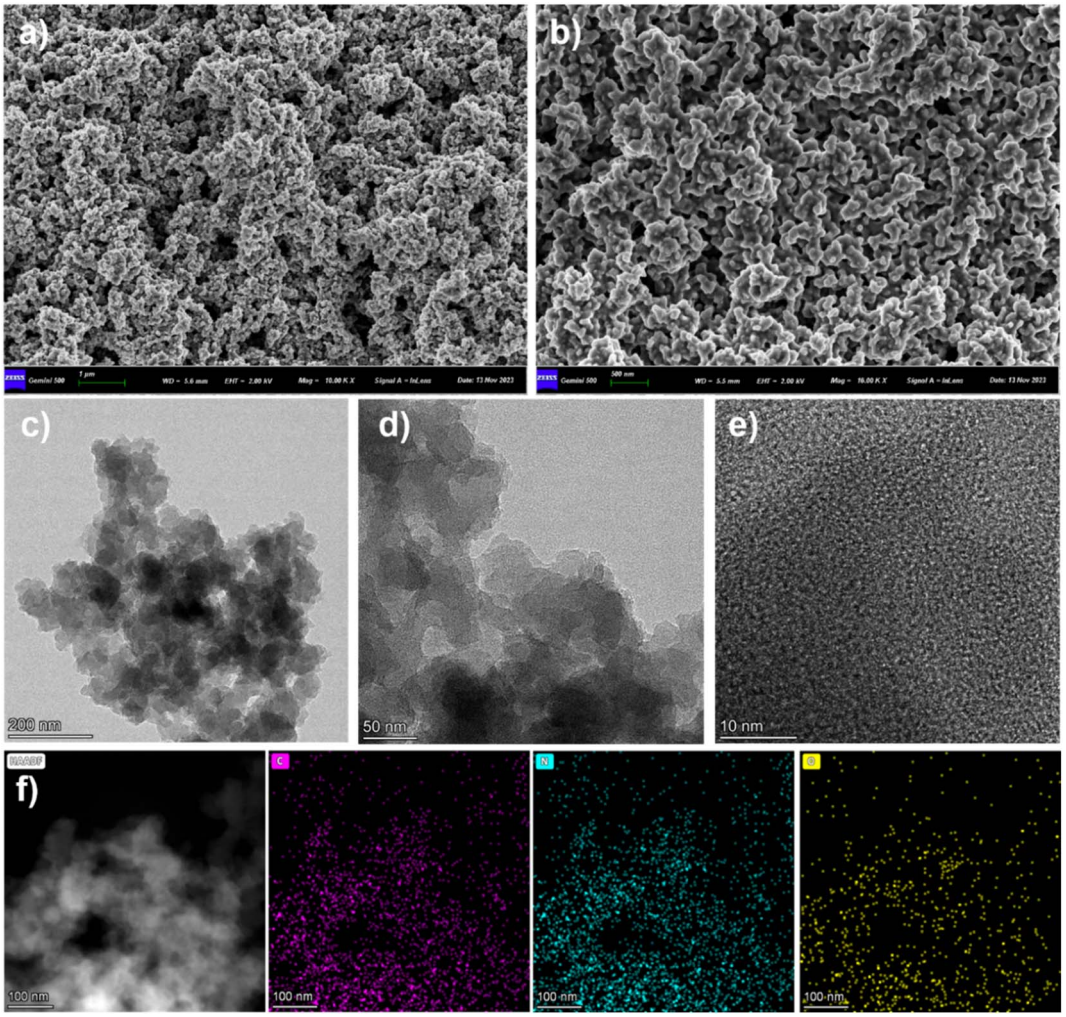

Fig. 2 Morphology characterization and elemental analysis of TPA-POR. (a and b) SEM images of TPA-POR at the scale bar of 1 μm and 500 nm, respectively; (c and d) TEM images of TPA-POR at varied scale bar of 200 nm, 50 nm respectively; (e) HR-TEM of TPA-POR at a scale bar of 10 nm; (f) the elemental mapping of TPA-POR.

was also visually testified by thermal image camera (Fig. 3f). With the variation of laser powers from 0.5 to 1.5 W cm^{-2}, the final temperature of TPA-POR (300 μg mL^{-1}) increased from 40.1 to 67 °C within 10 min of NIR irradiation. Subsequently, the recurrent heating and cooling experiment was carried out to estimate the photothermal reversibility of TPA-POR. As displayed in Fig. 3g, the TPA-POR possessed a high photothermal stability with almost unchanged maximum temperature after 4 cycles of NIR illumination. Subsequently, the photothermal conversion efficiency (η) of TPA-POR was quantified using eqn S1–S4, with key parameters derived from experimental data (τ_s = 233.58 s, as obtained from the cooling curve in Fig. 3h). The calculated η reached 80.47%, a value that significantly exceeds those of most previously reported photosensitizers (Table S1).[32] This remarkable performance can be attributed to the rationally designed D–A–D architecture of TPA-POR, which promotes efficient intramolecular charge separation and enhances non-radiative decay, thereby leading to superior photothermal conversion under NIR irradiation.[32]

The structural stability of TPA-POR was then evaluated across several conditions, beginning with its photothermal stability. This was measured by comparing the UV-vis absorption spectra before and after subjecting the material to multiple photothermal cycles. The observed near-overlap of the spectra, with minimal change (Fig. S5a), indicates that TPA-POR possesses good photothermal stability.[33] Water storage stability was assessed by comparing the photothermal performance of TPA-POR before and after 15 days of water immersion (Fig. S5b).[34] The results showed that its photothermal effect remained essentially unchanged, confirming excellent aqueous stability. Similarly, pH stability was evaluated by measuring the UV-vis absorption under different pH conditions (1.5–7.5) (Fig. S5c). TPA-POR also exhibited good stability across this pH range, with no significant change in absorption observed.[35]

Given the unique macromolecular structure of TPA-POR, in which the TPA moiety serves as an electron-donor core linked to triazine units, the porphyrin components are consistently characterized as electron donors and widely recognized as PSs.

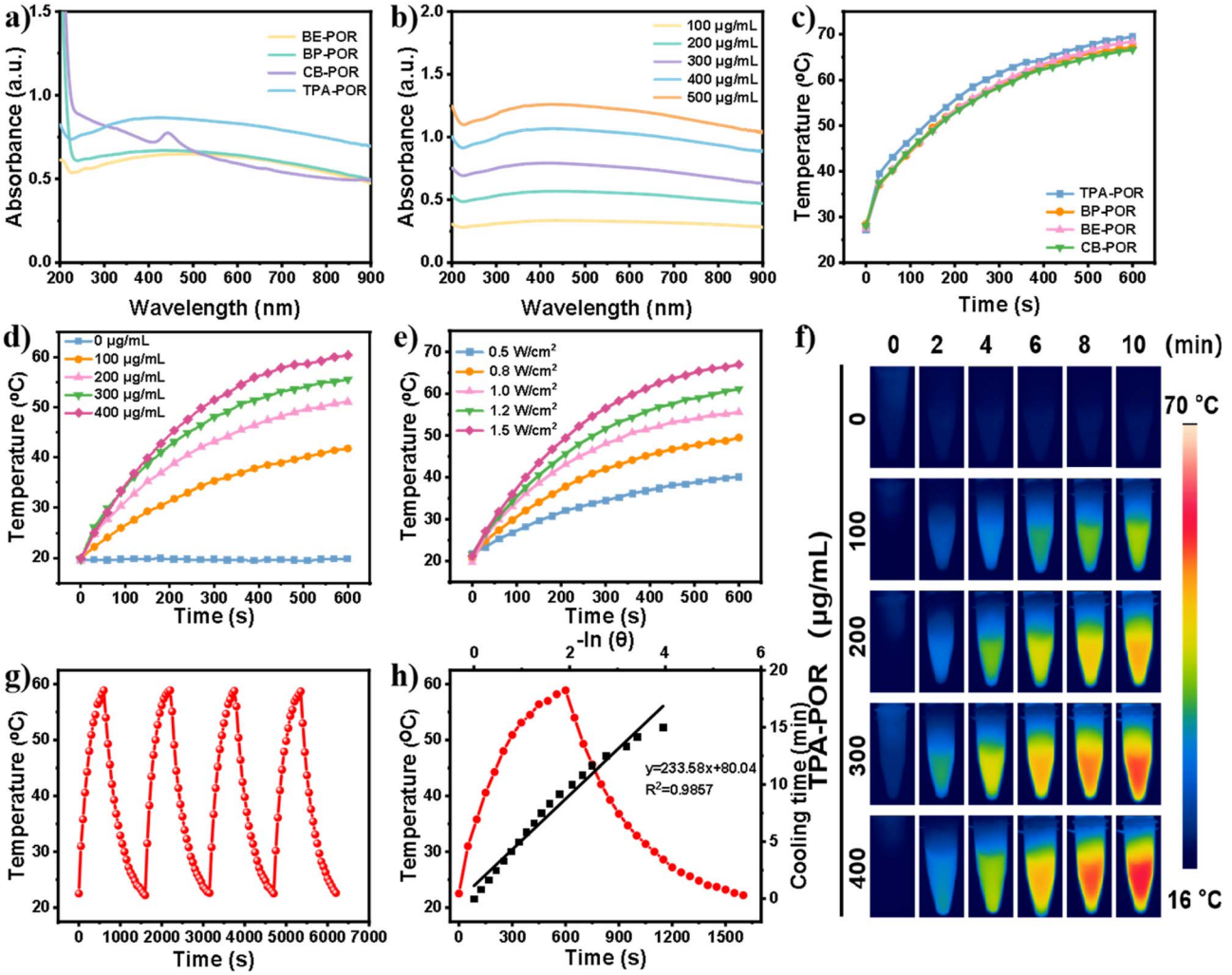

Fig. 3 Photophysical and photothermal characterization of the synthesized CMPs. (a) UV-vis absorption spectra of TPA-POR, CB-POR, BP-POR, and BE-POR at an equal concentration (300 μg mL^{-1}). (b) Concentration-dependent UV-vis absorption spectra of TPA-POR (100–500 μg mL^{-1}). (c) Photothermal heating curves of TPA-POR, CB-POR, BP-POR, and BE-POR under identical conditions (500 μg mL^{-1}, 808 nm, 1.0 W cm^{-2}). (d) Linear fitting of the steady-state temperature rise of TPA-POR as a function of concentration (0–400 μg mL^{-1}) after 10 min of NIR irradiation (808 nm, 1.0 W cm^{-2}). (e) Photothermal performance of TPA-POR under 808 nm laser irradiation at different power densities (0.5–1.5 W cm^{-2}). (f) Infrared thermal images of TPA-POR solutions at various concentrations and time points during irradiation. (g) Cyclic photothermal stability test of TPA-POR (300 μg mL^{-1}) over four on/off irradiation cycles. (h) Linear plot derived from the cooling stage, showing the negative natural logarithm of the temperature driving force *versus* time.

When covalently attached to a triazine unit, the porphyrin almost always functions as the electron donor under light irradiation, injecting electrons into the triazine moiety.[36] This strategic configuration results in a particularly robust donor–acceptor–donor (D–A–D) architecture. As a consequence, electrons in the photoactive TPA-POR are readily excited upon light exposure, leading to a significant enhancement of its photocatalytic activity.[37] Accordingly, the ability of TPA-POR to generate cytotoxic ROS under NIR irradiation was evaluated using both Electron Paramagnetic Resonance (EPR) spectroscopy and chemical colorimetric assays. All experiments were conducted under ambient conditions to enhance the clinical relevance and better simulate a natural treatment environment.[38] A 2,7-dichlorofluorescein diacetate (DCFH) probe was used to assess the total ROS generation capacity of TPA-POR. The results (Fig. S6) revealed that the fluorescence intensity of the probe alone increased only minimally upon laser irradiation. However, upon the addition of TPA-POR, a substantial increase in fluorescence intensity was noted, indicating TPA-POR possessed excellent photodynamic performance.[39] Subsequently, the EPR spectroscopy were conducted to monitor the PDT process catalyzed by TPA-POR. As illustrated in Fig. 4a–c, TPA-POR was capable of generating ROS through two distinct pathways under NIR irradiation. These pathways encompassed the formation of oxygen-independent hydroxyl radicals (˙OH, type I) and superoxide anions (O_2^-, also type I), as well as the production of oxygen-dependent singlet oxygen ($^1O_2$, type II), simultaneously.[40]

Furthermore, the generated ROS were quantified and identified by employing diphenyl benzofuran (DPBF), Methyl Blue

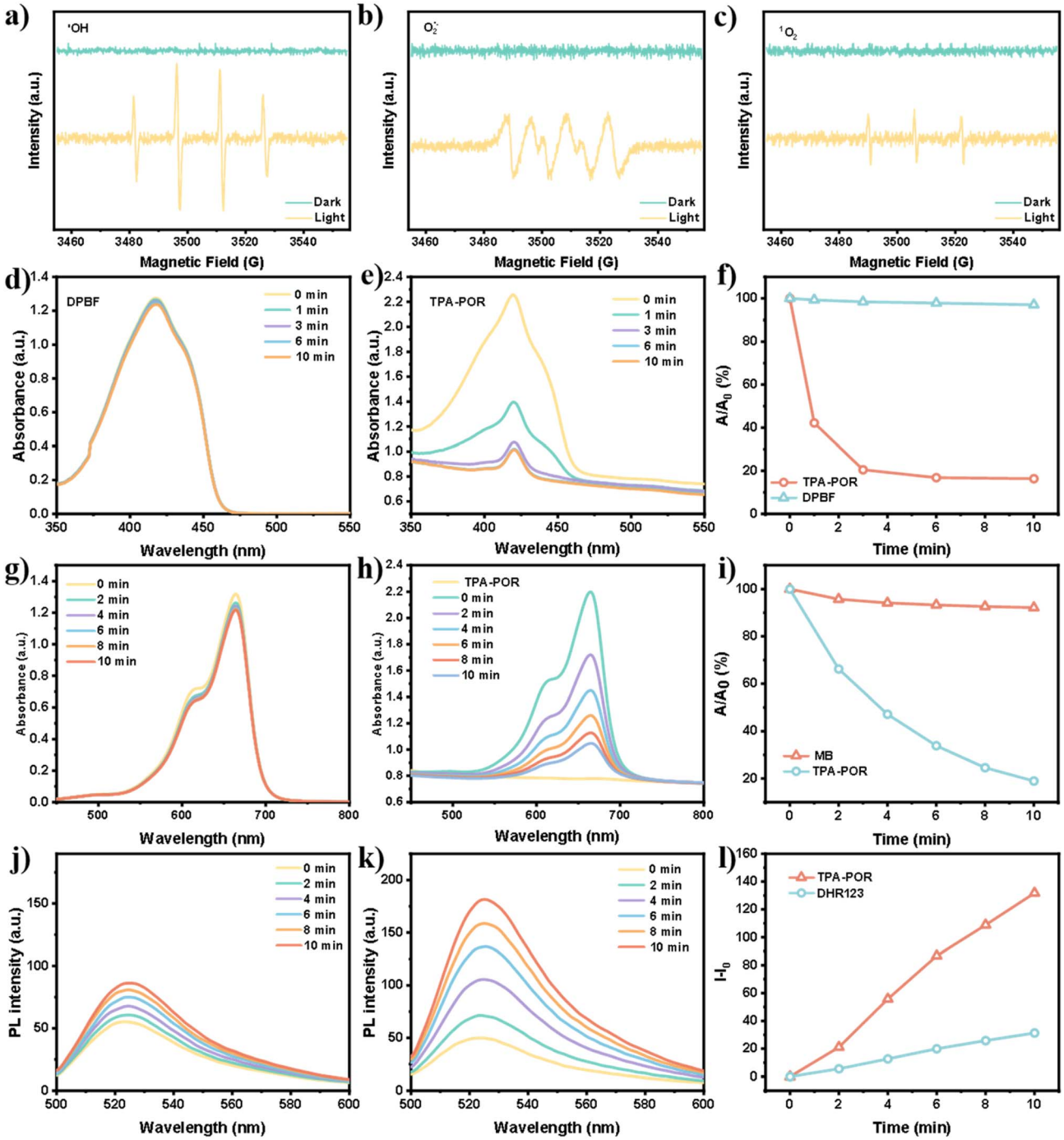

Fig. 4 Detection and quantification of photogenerated ROS. (a) EPR spectra of TPA-POR with TEMP in CH_3CN under dark and NIR irradiation; (b) EPR spectra of TPA-POR with DMPO in H_2O under dark and NIR irradiation; (c) EPR spectra of TPA-POR with DMPO in CH_3CN under dark and NIR irradiation; UV-vis spectra of (d) DPBF, (e) TPA-POR under NIR (1.0 W cm^{-2}) irradiation; (f) comparison of the decay rates of DPBF induced by TPA-POR under NIR (1.0 W cm^{-2}) irradiation; (g) UV-vis spectra of MB under NIR irradiation; (h) UV-vis spectra of MB with TPA-POR under NIR irradiation; (i) comparison of the decay rate of MB induced by TPA-POR under NIR irradiation; (j) FL spectra of DHR123 under NIR irradiation; (k) FL spectra of DHR123 with TPA-POR under NIR irradiation; (l) comparison of the decay rate of DHR123 induced by TPA-POR under NIR irradiation.

(MB), and dihydrorhodamine (DHR123) as specific probes for singlet oxygen $^1O_2$, $^{\cdot}OH$ and $O_2^{\cdot-}$, respectively. Compared with the slight decay of DPBF (Fig. 4d) under the NIR illumination, a much significant decreases in DPBF absorbance were observed after the addition of TPA-POR (Fig. 4e). Upon the treatment of TPA-POR, the absorbance of DPBF was rapidly decreased by 57.8% within 1 min of illumination, which further decreased to 83.64% after 10 min of irradiation. These results suggested TPA-POR could rapidly convert the surrounding O_2 to generate $^1O_2$ when irradiated with a 808 nm NIR (1.0 W cm^{-2}).[41]

As delivered in Fig. 4g–i, the UV-vis absorbance of MB also decreased quite weakly under NIR irradiation alone, but the absorption of MB was significantly decreased after the addition of TPA-POR. Specifically, the absorbance decreased by 81.05% within 10 min of NIR irradiation, demonstrating the strong $^{\bullet}OH$ generation ability of TPA-POR under NIR irradiation *via* directly sensitizing water.[42] Moreover, the experimental results in Fig. 4j–l indicated the fluorescence intensity of the pure DHR123 only increased by only 31.32% under NIR irradiation for 10 min. However, the fluorescence intensity was increased significantly by 131.76% after the addition of TPA-POR, indicating the excellent O_2^- production ability.[43] The above results indicated TPA-POR featured both type I (oxygen-dependent) and type II (oxygen-independent) photodynamic capacities, which could exert sterilization not only in an aerobic environment, but also kill bacteria in an anoxic environment, demonstrating the superb phototherapeutic antimicrobial prospect.

Given its promising photothermal and photodynamic properties, we conducted a comprehensive investigation into the antimicrobial potential of TPA-POR. We used *Escherichia coli* (*E. coli*) and *Staphylococcus aureus* (*S. aureus*) as model Gram-negative and Gram-positive bacteria, respectively (Fig. S7). After 10 min of NIR irradiation (1.0 W cm^{-2}), the number of bacterial colonies was gradually decreased with the increase of TPA-POR dose. The killing ability of TPA-POR (300 μg mL^{-1}) reached 99.7 ± 0.26% and 98.3 ± 0.12% against *E. coli* and *S. aureus*, respectively. To probe the antibacterial mechanism, we established a series of experimental groups for each bacterial strain, varying the conditions of TPA-POR and light exposure. As depicted in Fig. 5a and b, the number of colonies of both *E. coli* and *S. aureus* in the PBS and PBS + NIR groups remained largely unchanged, indicating the NIR irradiation alone has no significant effect on bacterial growth. By contrast, the survival rate of *E. coli* and *S. aureus* treated by TPA-POR alone also showed a decrease of 12.53% ± 6.18 and 20.8 ± 3.68%, respectively. However, the infliction of NIR to the TPA-POR induced substantial reductions in the bacteria number, with *E. coli* and *S. aureus* decreasing by 99.54 ± 0.18% and 98.02 ± 1.10%, respectively. This results revealed the D–A–D structure could effectively eliminate the differences in resistance to PDT and PTT induced by the distinct cell structures of different bacteria.[44]

To further confirm these results, TEM was performed on the bacteria strains underwent varied treatments.[45] As shown in Fig. 5c, bacterial electron microscopy revealed *E. coli* and *S. aureus* in the PBS and PBS + NIR groups featured overall bacterial structural integrity with smooth appearance and evident flagella. Remarkably, when bacteria were grown on the surface of TPA-POR and subjected to NIR irradiation, extensive damage was observed. This included obvious cytoplasmic efflux, cell wall breakage, and the absence of flagella. By contrast, only slight bacterial damage was observed in the TPA-POR group, which was consistent with the bacterial smear plate results. Live-dead staining (Fig. 5d) results of *E. coli* and *S. aureus* showed identical results with the TEM observations, from which, TPA-POR-treated bacteria were all stained with red fluorescence. All these results demonstrated the antimicrobial properties of TPA-POR were ascribed to the additive effect of proposed D–A–D structure with PTT and PDT.[46–48]

Then, the biocompatibility of TPA-POR was assessed by hemolysis and cytotoxicity assays. The hemolysis analysis was performed to estimate the toxicity of TPA-POR on red blood cells, using water and PBS as positive control and negative control, respectively.[49] As displayed in Fig. 6a, TPA-POR was benign to the red blood cells with a qualified hemolysis rate below 1.5% over the experimental range (100–500 μg mL^{-1}). The cytotoxicity experiments were carried out to evaluate the effect of TPA-POR on the viability of normal cells *via* the MTT method, using Human Liver-7702 (HL7702) and Human embryonic kidney 293 (HEK 293) cells as models.[50] The MTT results demonstrated a concentration-dependent cytotoxicity of TPA-POR, and the exertion of NIR illumination induced the increase of cytotoxicity. However, the viabilities of HL7702 and HEK293 cells were well retained exceeding 80% (Fig. 6b and c) at the optimal therapeutic concentration (300 μg mL^{-1}) regardless of NIR illuminations. The consequences suggested TPA-POR possessed a favorable *in vitro* safety profile at its optimal antimicrobial concentration. To investigate the potential impact of TPA-POR on cellular migratory capacity, cell scratching experiments were we conducted utilizing mouse fibroblasts as our model system (Fig. S8). Cell migration assays showed that TPA-POR (300 μg mL^{-1}) did not significantly affect normal cell mobility after 12 h or 24 h of co-culture. The migration rates were comparable to the control, measuring 58.7 ± 0.75% (TPA-POR) *versus* 59.3 ± 1.95% (control) at 24 h, confirming its negligible impact on migratory capability. To assess the antimicrobial effectiveness and wound healing capabilities of TPA-POR *in vivo*, mouse models with *S. aureus*-infected back wounds was established.[51] Female BALB/c mice (6–8 weeks old, $n = 3$ per group) were randomly divided into four treatment groups, including the PBS, PBS + NIR, TPA-POR, and TPA-POR + NIR. The group size was determined with reference to common practice in similar published studies on infected wound healing in murine models and in accordance with the principle of using the minimum number of animals necessary to obtain scientifically valid results. For wound modeling, full-thickness skin wounds were created on the dorsal surface using an 8 mm punch biopsy. After infection was established, mice were randomized into treatment groups *via* a computer-generated sequence to ensure balanced distributions of body weight and initial wound size across all groups. Throughout the experiment and data analysis, investigators performing wound area measurements, bacterial colony counts, and histological assessments were blinded to group assignments to minimize bias. All animal procedures were approved by the Institutional Animal Care and Use Committee (IACUC) of Shandong Second Medical University (Approval No. 2022SDL150) and conducted in compliance with the National Institutes of Health Guide for the Care and Use of Laboratory Animals. The treatment conditions included the application of TPA-POR at a concentration of 300 μg mL^{-1}, the use of H_2O_2 at 8.82 mM, and laser irradiation at 808 nm (1.0 W cm^{-2} for 10 min) in the respective groups.

Treatments were given on the 1st and 3rd days, while wound sizes were recorded and photographed on days 0, 2, 4, 6, and 8,

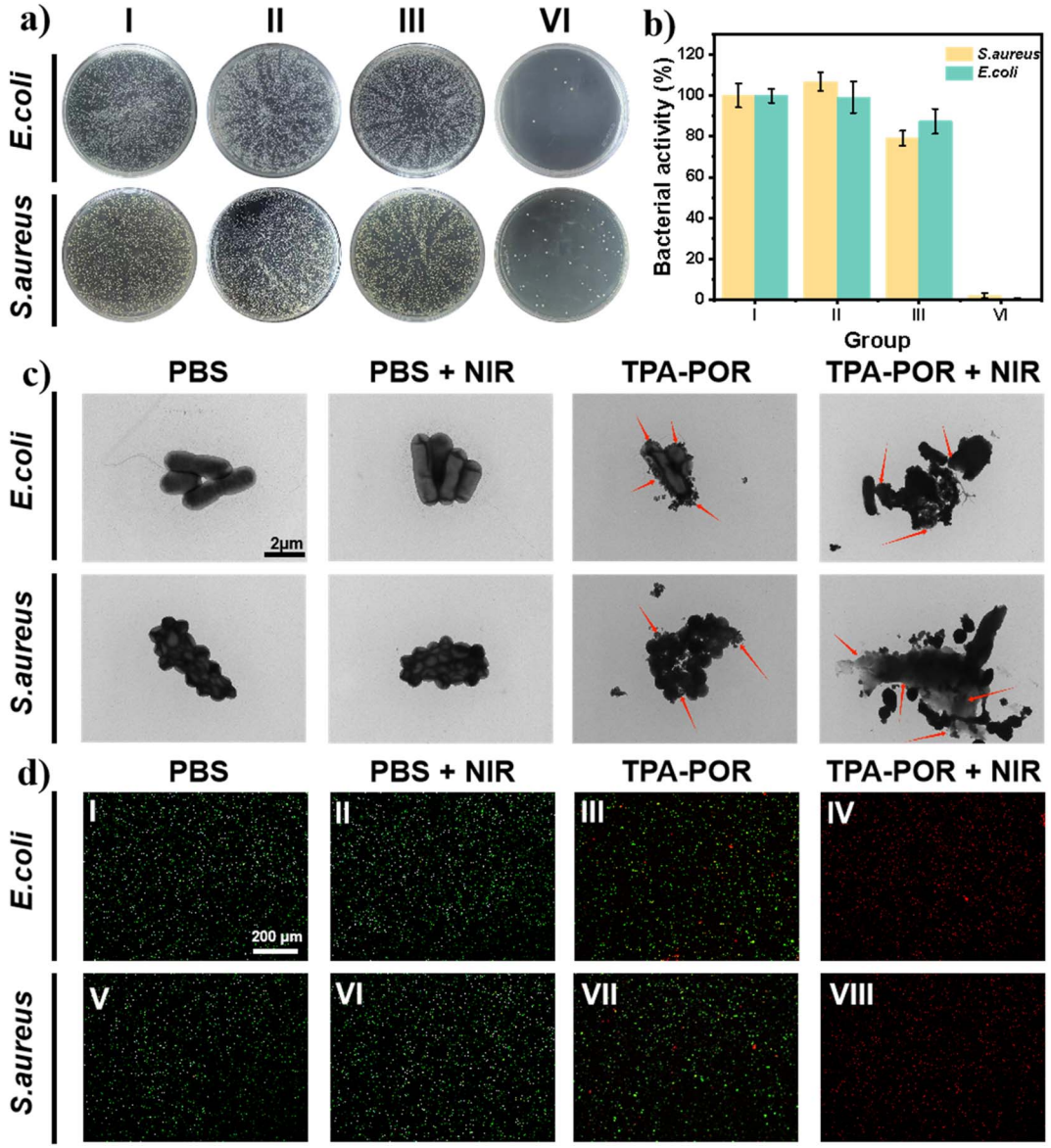

Fig. 5 (a) Antibacterial performance of TPA-POR (300 μg mL^{-1}), photographs of remaining *E. coli* and *S. aureus* colonies on agar plates in four groups (Group I: PBS, Group II: PBS + NIR, III: TPA-POR, Group IV: TPA-POR + NIR); (b) corresponding bacterial viability of *E. coli* and *S. aureus* after different treatments in the four groups; (c) TEM images of treated *E. coli* and *S. aureus* in the four group; (d) SYTO9/PI staining images of *E. coli* and *S. aureus* under different treatments in the eight groups. Data are presented as mean ± standard deviation (SD) from three independent biological replicates ($n = 3$).

respectively. Upon completing the modeling process (on day 1), all wounds exhibited signs of infection, including visible pus, and dense bacterial population revealed by the bacterial smear plates at the wound sites (Fig. 6d). These results confirmed the successful creation of a *S. aureus*-infected mouse wound model.[52] Additionally, an infrared camera was utilized to monitor the temperature change of wound sites during NIR irradiation treatment (Fig. S9). These results showed the temperature of wounds treated with TPA-POR could reach up to 55.8 °C, which is adequate to effectively destroy bacteria. In contrast, the temperature of wounds in the PBS group remained around 31.7 °C, while the PBS + NIR group reached only approximately 35.5 °C. The NIR-illumination-induced sterilizing effect could also be directly reflected by the results of bacterial smear plates at the wound sites (Fig. 6e). As seen, the treatment with TPA-POR alone resulted in a 13.27 ± 2.62% reduction in the number of bacterial colonies, while the TPA-POR + NIR group showed the least number of colonies with a reduction of 91.21 ± 1.42%. The wounds of mice under varied treatments were gradually decreased with the extension of time. The wound area of mice treated with TPA-POR + NIR was smaller than those treated by others. And the progression of wound healing in the different groups of mice could also be illustrated from the simulations of the wound area on days 0, 2, 4, 6 and 8 (Fig. 6f). The quantification of wound areas revealed significant differences between the treated and control groups

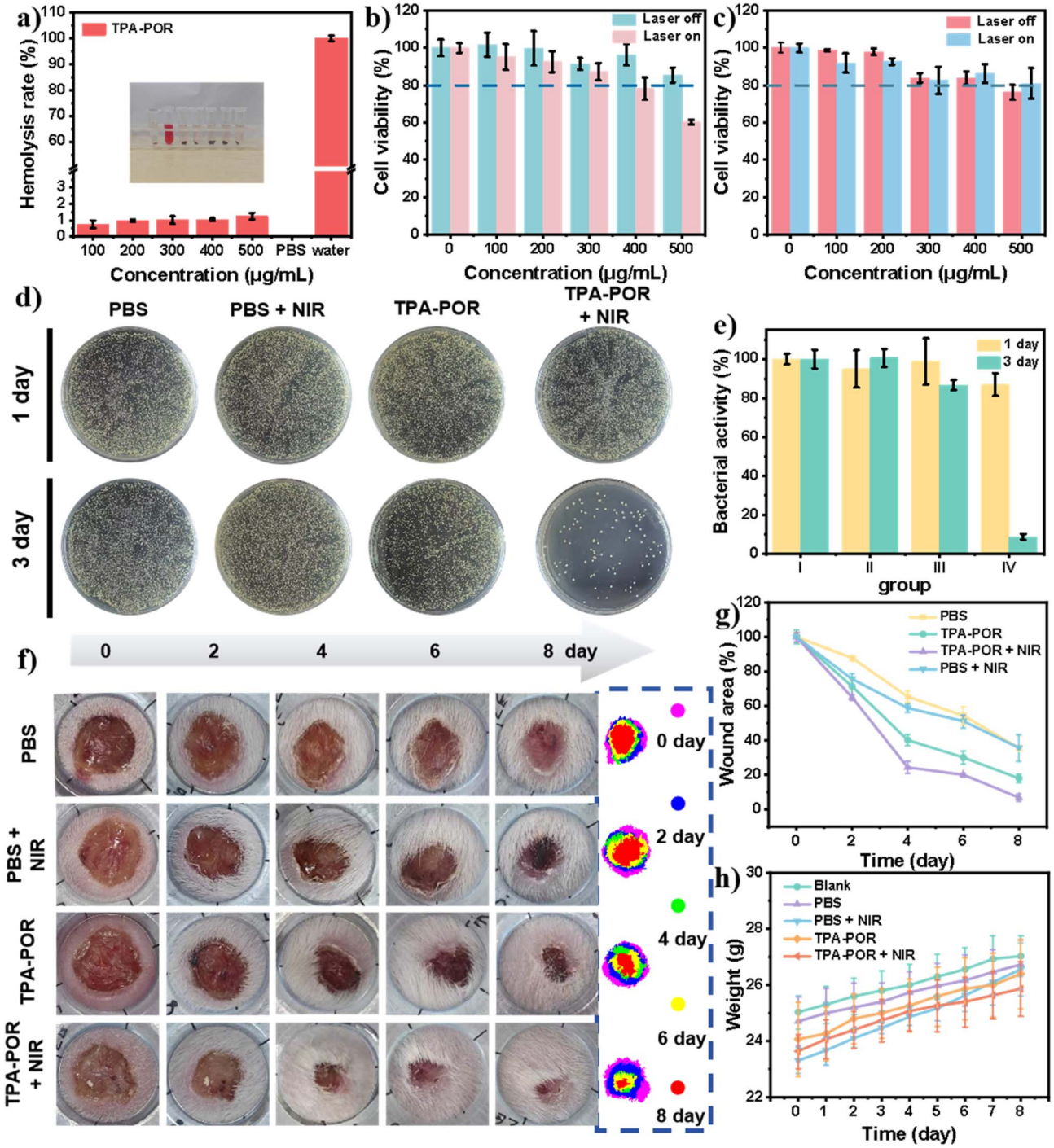

Fig. 6 (a) Hemolytic activity assessment of TPA-POR; (b) cytotoxicity of TPA-POR on HEK 293; (c) cytotoxicity of TPA-POR on HL7702; (d) bacterial cultures at the wound sites on the 1st and 3rd day; (e) quantification of bacterial cultures at wound sites on the 1st and 3rd day; (f) representative photos of corresponding wound area of five groups on days of 0, 2, 4, 6 and 8 days; the right is the traces of wound-bed closure during treatments; (g) wound healing rate of the four groups during treatment; (h) weight change of the five groups during treatment. All quantitative data are presented as mean ± standard deviation (SD, $n = 3$).

(Fig. 6g). Specifically, on day 4, mice in the treated group exhibited notably smaller wound areas compared to the PBS group. The most striking reduction was observed in the TPA-POR + NIR group, with a decrease of 75.71 ± 3.37% in wound size (*vs.* PBS, PBS + NIR and TPA-POR for 34.55 ± 3.21%, 41.17 ± 2.39% and 59.85 ± 3.19%). By day 6, the healing trends became even more apparent, with the TPA-POR + NIR group achieving an 80.04 ± 1.07% wound area reduction (*vs.* PBS, PBS + NIR and TPA-POR for 45.65 ± 5.40%, 48.84 ± 3.80% and 69.95 ± 3.70%). Remarkably, at the end of the treatment, the TPA-POR + NIR

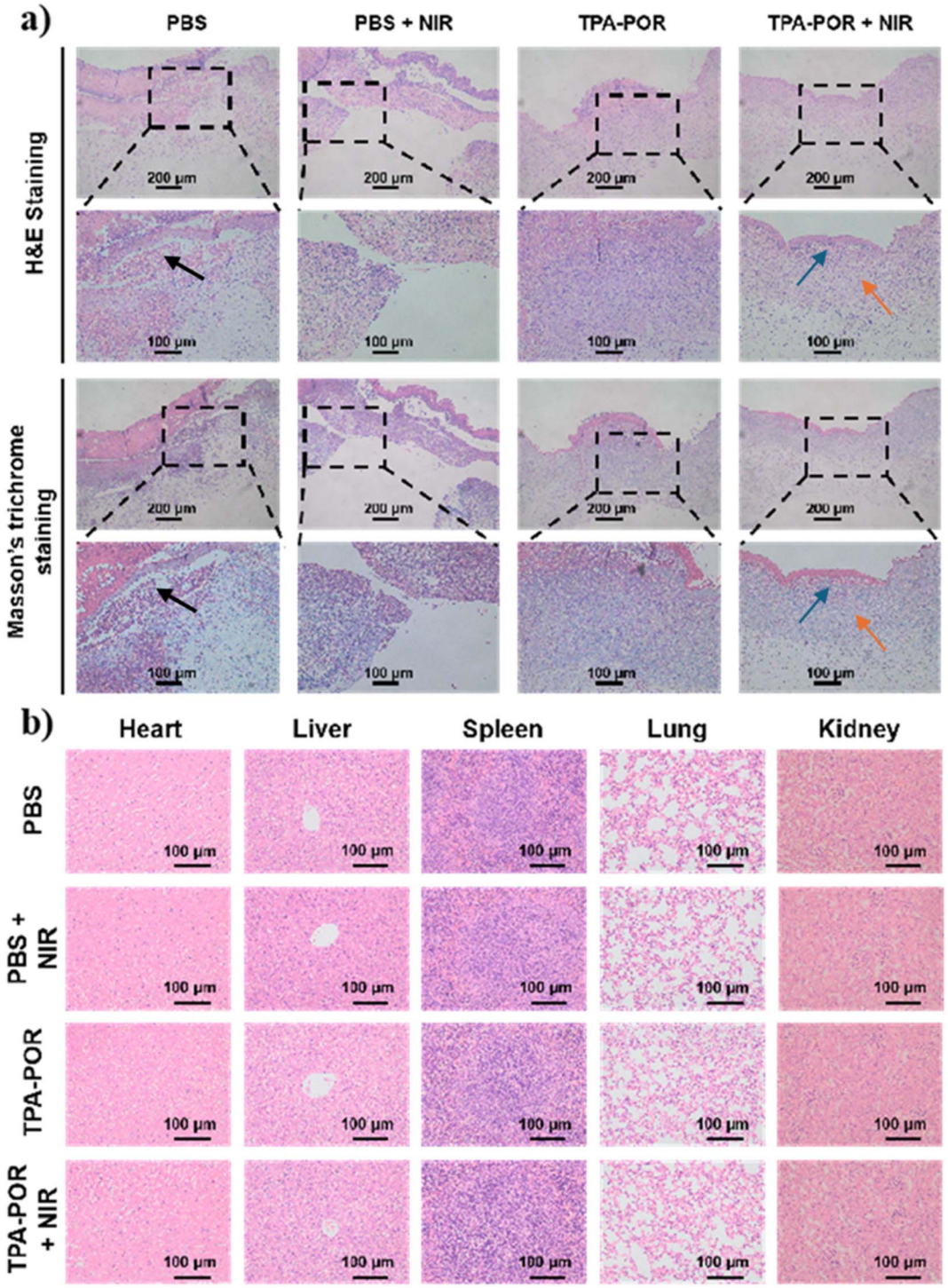

Fig. 7 (a) H&E stained wound tissue sections for the four groups on day 8. Key histological structures are indicated with colored arrows: inflammatory exudate (black arrows), the presence of new hair follicles (orange arrows), and the regenerated epidermis (blue arrows). The scale bar applies to all images; (b) tissue (heart, liver, spleen, lung and kidney) slices stained with H&E from five groups. The scale bar in the first column applies to all images.

group had only a 6.89 ± 2.07% remaining wound area, much lower than the other groups (35.98 ± 4.47%, 35.52 ± 7.18%, and 17.95 ± 2.42% for PBS, PBS + NIR, and TPA-POR, respectively). Taken together, the excellent *in vivo* wound healing outcomes confirm the translational potential of TPA-POR for combating *S. aureus* infections. Its ability to synergize multiple antimicrobial mechanisms effectively addresses the challenges of hypoxic and biofilm-associated wounds. Furthermore, this strong therapeutic performance is supported by a high safety margin. Toxicity evaluations, based on body weight monitoring during

treatment, revealed that mice receiving TPA-POR (with or without NIR) showed a steady growth trend comparable to the PBS group (Fig. 6h), confirming its minimal systemic toxicity.[53] These results underscore TPA-POR's balanced profile of potent efficacy and good biocompatibility, advocating for its future clinical development.[53]

After the treatment, histological analysis was performed to evaluate the healing status of the wound and to assess potential lesions in major organs (heart, liver, spleen, lungs, and kidneys) in each experimental group.[54] As shown in Fig. 7a, wounds in the PBS-treated groups, with or without NIR irradiation, displayed incomplete skin coverage, significant inflammatory cell infiltration, and a lack of organized angiogenesis within the scar tissue, indicating delayed wound healing. In the TPA-POR group without laser exposure, the wound area showed a more intact skin architecture compared to the PBS controls, though residual scarring and moderate inflammation were still observable. Most notably, wounds treated with TPA-POR + NIR exhibited near-complete re-epithelialization, as indicated by the continuous and well-regenerated epidermal layer (blue arrows). Furthermore, the presence of new hair follicles (orange arrows) and the almost the disappearance of inflammatory exudate (black arrows) suggest active tissue regeneration and resolution of infection, aligning with the enhanced antibacterial effect observed *in vivo*. These histological findings corroborate the macroscopic wound healing results and further confirm the efficacy of TPA-POR-mediated photothermal therapy in promoting the repair of infected wounds. Simultaneously, histopathological assessment of major organs revealed no significant signs of toxicity across all treatment groups (Fig. 7b). Tissues from the heart, liver, spleen, lungs, and kidneys of mice treated with TPA-POR, with or without NIR, displayed normal cellular architecture, with no evidence of apoptosis, necrosis, inflammatory lesions, or other pathological alterations compared to the PBS control groups. These results, consistent with the serum biochemical indices presented in Fig. S10, demonstrate the good biocompatibility and minimal systemic toxicity of TPA-POR following *in vivo* administration.[55] Collectively, the data from Fig. 7 underscore the dual advantage of TPA-POR, which effectively accelerates infected wound healing while maintaining a favorable safety profile, thereby highlighting its potential as a promising photothermally activated antimicrobial agent for translational applications.

Conclusion

In summary, this work presents TPA-POR, a conjugated microporous polymer photosensitizer engineered to treat wound infections. Its design is based on a rational conjugation-bridge strategy that yields a rigid, distorted porous framework to suppress porphyrin aggregation and a D–A–D topology. This unique structure endows the material with multiple key functions, including facilitating intramolecular charge separation to enhance photodynamics, providing an inherent positive charge for targeting bacterial membranes, and exhibiting synergistic photothermal–photodynamic activity under 808 nm irradiation. Most critically, the dual Type I/II photodynamic mechanism ensures effective ROS production even in hypoxia. These integrated features enable TPA-POR to achieve potent antibacterial killing against both *S. aureus* and *E. coli in vitro*. The therapeutic promise is conclusively validated *in vivo*, where TPA-POR-mediated phototherapy effectively clears *S. aureus* infection and robustly promotes wound healing. This study thus establishes a new paradigm for designing solid-state photosensitizers *via* the integration of anti-quenching porous scaffolds with multifunctional D–A–D architectures.

Conflicts of interest

There are no conflicts to declare.

Data availability

Data will be made available on request.

Supplementary information (SI): additional experimental details, materials, general instruments, methods, physical characterizations, photo-physical performance, the stability test, TEM and other details, as well as supporting tables and references. See DOI: https://doi.org/10.1039/d5ra09715k.

References

1 G. Y. Guo, H. L. Zhang, H. Shen, C. Z. Zhu, R. K. He, J. Tang, Y. Wang, X. W. Jiang, J. X. Wang, W. B. Bu and X. L. Zhang, Space-Selective Chemodynamic Therapy of $CuFe_5O_8$ Nanocubes for Implant-Related Infections, *ACS Nano*, 2020, **14**, 13391–13405.
2 D. Sun, X. Pang, Y. Cheng, J. Ming, S. J. Xiang, C. Zhang, P. Lv, C. C. Chu, X. L. Chen, G. Liu and N. F. Zheng, Ultrasound-switchable nanozyme augments sonodynamic therapy against multidrug-resistant bacterial infection, *ACS Nano*, 2020, **14**, 2063–2076.
3 P. P. Kalelkar, M. Riddick and A. J. García, Biomaterial-based antimicrobial therapies for the treatment of bacterial infections, *Nat. Rev. Mater.*, 2022, **7**, 39–54.
4 N. D. Friedman, E. Temkin and Y. Carmeli, The negative impact of antibiotic resistance, *Clin. Microbiol. Infect.*, 2016, **22**, 416–422.
5 Z. Xing, J. Guo, Z. Wu, C. He, L. Wang, M. Bai, X. Liu, B. Zhu, Q. Guan and C. Cheng, Nanomaterials-Enabled physicochemical antibacterial therapeutics: toward the antibiotic-free disinfections, *Small*, 2023, **19**, b2303594.
6 X. Hu, H. Zhang, Y. Wang, B. C. Shiu, J. H. Lin, S. Zhang, C. W. Lou and T. T. Li, Synergistic antibacterial strategy based on photodynamic therapy: Progress and perspectives, *Chem. Eng. J.*, 2022, **450**, 138129.
7 M. Tavakkoli Yaraki, B. Liu and Y. N. Tan, Emerging strategies in enhancing singlet oxygen generation of nano-photosensitizers toward advanced phototherapy, *Nano-Micro Lett.*, 2022, **14**, 123.
8 Y. Zhang, B. T. Doan and G. Gasser, Metal-based photosensitizers as inducers of regulated cell death mechanisms, *Chem. Rev.*, 2023, **123**, 10135–10155.

9 F. Glaser, A. Aydogan, B. Elias and L. Troian-Gautier, The great strides of iron photosensitizers for contemporary organic photoredox catalysis: On our way to the holy grail?, *Coord. Chem. Rev.*, 2024, **500**, 215522.

10 F. Schnetz, I. Knysh, D. Jacquemin, S. A. Andaloussi, M. Presset, S. Lajnef, F. Peyrot and D. L. Versace, Porphyrin-based photosensitizers for visible-light polymerization and antibacterial applications, *Polym. Chem.*, 2024, **15**, 1377–1392.

11 K. Huang, M. Yan, H. Zhang, J. Xue and J. Chen, A phthalocyanine-based photosensitizer for effectively combating triple negative breast cancer with enhanced photodynamic anticancer activity and immune response, *Eur. J. Med. Chem.*, 2022, **241**, 114644.

12 Q. Cheng, X. Guo, X. Hao, Z. Shi, S. Zhu and Z. Cui, Fabrication of robust antibacterial coatings based on an organic–inorganic hybrid system, *ACS Appl. Mater. Interfaces*, 2019, **11**, 42607–42615.

13 V. N. Nguyen, Z. Zhao, B. Z. Tang and J. Yoon, Organic photosensitizers for antimicrobial phototherapy, *Chem. Soc. Rev.*, 2022, **51**, 3324–3340.

14 G. Liu, H. Wang, C. Shi, G. Chen, Y. Wang, W. Huang and H. Zhao, Confining isolated photosensitizers to relieve self-aggregation and potentiate photodynamic efficacy for synergistic cancer therapy, *Chem. Commun.*, 2022, **58**, 10813–10816.

15 W. Wu and B. Liu, Modulating the optical properties and functions of organic molecules through polymerization, *Mater. Horiz.*, 2022, **9**, 99–111.

16 A. Hayat, M. Sohail, A. ElJery, K. M. Al-Zaydi, S. Raza, H. Ali, Y. AL-Hadeethi, T. A. Taha, I. Din, M. A. Khan, M. A. Amin, E. Ghasali, Y. Orooji, Z. Ajmal and M. Z. Ansari, Recent advances in ground-breaking conjugated microporous polymers-based materials, their synthesis, modification and potential applications, *Mater. Today*, 2023, **64**, 180–208.

17 R. Azizi, M. Kermanian, V. Alinezhad, A. Kalantari-Hesari, S. Yousefiasl, L. Maeso, G. Orive, A. Mohammadi, K. Esmaeilzadeh, M. Seyedhamzeh, F. Almasib and A. Maleki, *J. Mater. Chem. B*, 2025, **13**, 9228–9242.

18 J. X. Jiang, F. Su, A. Trewin, C. D. Wood, N. L. Campbell, H. Niu, C. Dickinson, A. Y. Ganin, M. J. Rosseinsky and Y. Z. Khimyak, Conjugated microporous poly (Aryleneethynylene) networks, *Angew. Chem., Int. Ed.*, 2007, **46**, 8574–8578.

19 Y. Wang, Q. Yuan, M. Li and Y. Tang, Cationic conjugated microporous polymers coating for dual-modal antimicrobial inactivation with self-sterilization and reusability functions, *Adv. Funct. Mater.*, 2023, **33**, 2213440.

20 V. N. Nguyen, Y. Yan, J. Zhao and J. Yoon, Heavy-atom-free photosensitizers: from molecular design to applications in the photodynamic therapy of cancer, *Acc. Chem. Res.*, 2020, **54**, 207–220.

21 B. C. Ma, S. Ghasimi, K. Landfester and K. A. I. Zhang, Enhanced visible light promoted antibacterial efficiency of conjugated microporous polymer nanoparticles via molecular doping, *J. Mater. Chem. B*, 2016, **4**, 5112–5118.

22 Z. Li, X. Feng, S. Gao, Y. Jin, W. Zhao, H. Liu, X. Yang, S. Hu, K. Cheng and J. Zhang, Porous organic polymer-coated band-Aids for Phototherapy of Bacteria-Induced Wound Infection, *ACS Appl. Bio Mater.*, 2019, **2**, 613–618.

23 X. H. Han, K. Gong, X. Huang, J. W. Yang, X. Feng, J. Xie and B. Wang, Syntheses of covalent organic frameworks via a one-pot Suzuki coupling and Schiff's base reaction for C_2H_4/C_3H_6 separation, *Angew. Chem., Int. Ed.*, 2022, **61**, e202202912.

24 T. Wang, L. Zhang, J. Gu, J. Liu, Z. Liu, Y. Xie, H. Liu, L. Zhang and Z. A. Qiao, Competition among refined hollow structures in Schiff base polymer derived carbon microspheres, *Nano Lett.*, 2022, **22**, 3691–3698.

25 L. G. Ding, S. Wang, B. J. Yao, F. Li, Y. A. Li, G. Y. Zhao and Y. B. Dong, Synergistic antibacterial and anti-Inflammatory effects of a drug-Loaded self-standing porphyrin-COF membrane for efficient skin wound healing, *Adv. Healthcare Mater.*, 2021, **10**, 2001821.

26 Y. Sheng, X. Sun, J. Han, W. Hong, J. Feng, S. Xie, Y. Li, F. Yan, K. Li and B. Tian, N-acetylcysteine functionalized chitosan oligosaccharide-palmitic acid conjugate enhances ophthalmic delivery of flurbiprofen and its mechanisms, *Carbohydr. Polym.*, 2022, **291**, 119552.

27 S. Ahlawat, K. R. Mote, N. A. Lakomek and V. Agarwal, Solid-state NMR: Methods for biological solids, *Chem. Rev.*, 2022, **122**, 9643–9737.

28 H. A. Nel, A. J. Chetwynd, C. A. Kelly, C. Stark, E. Valsami-Jones, S. Krause and I. Lynch, An untargeted thermogravimetric analysis-fourier transform infrared-gas chromatography-mass spectrometry approach for plastic polymer identification, *Environ. Sci. Technol.*, 2021, **55**, 8721–8729.

29 N. Chaoui, M. Trunk, R. Dawson, J. Schmidt and A. Thomas, Trends and challenges for microporous polymers, *Chem. Soc. Rev.*, 2017, **46**, 3302–3321.

30 O. Santoro and L. Izzo, Antimicrobial polymer surfaces containing quaternary ammonium centers (QACs): synthesis and mechanism of action, *Int. J. Mol. Sci.*, 2024, **25**, 7587.

31 Z. Xie, W. Wang, X. Ke, X. Cai, X. Chen, S. Wang, W. Lin and X. Wang, A heptazine-based polymer photocatalyst with donor-acceptor configuration to promote exciton dissociation and charge separation, *Appl. Catal., B*, 2023, **325**, 122312.

32 R. L. Ge, P. N. Yan, Y. Liu, Z. S. Li, S. Q. Shen and Y. Yu, Recent advances and clinical potential of near infrared photothermal conversion materials for photothermal hepatocellular carcinoma therapy, *Adv. Funct. Mater.*, 2023, **33**, 2301138.

33 Y. Yang, L. Yang, F. Yang, W. Bai, X. Zhang, H. Li, G. Duan, Y. Xu and Y. Li, A bioinspired antibacterial and photothermal membrane for stable and durable clean water remediation, *Mater. Horiz.*, 2023, **10**, 268–276.

34 Y. Liu, T. Chen, Z. Jin, M. Li, D. Zhang, L. Duan, Z. Zhao and C. Wang, Tough, stable and self-healing luminescent perovskite-polymer matrix applicable to all harsh aquatic environments, *Nat. Commun.*, 2022, **13**, 1338.

35 N. Song, S. Ren, Y. Zhang, C. Wang and X. Lu, Confinement of prussian blue analogs boxes inside conducting polymer nanotubes enables significantly enhanced catalytic performance for water treatment, *Adv. Funct. Mater.*, 2022, **32**, 2204751.

36 S. Singh, M. K. Ghorai and K. K. Kar, A cobalt harnessed phenanthroline and triphenylamine-based conjugated mesoporous polymer designed by a donor–acceptor approach for trifunctional electrocatalysis, *J. Mater. Chem. A*, 2023, **11**, 20290–20301.

37 C. Cui, X. Zhao, X. Su, N. Xi, X. Wang, X. Yu, X. Zhang, H. Liu and Y. Sang, Porphyrin-based donor–acceptor covalent organic polymer/$ZnIn_2S_4$ Z-Scheme heterostructure for efficient photocatalytic hydrogen evolution, *Adv. Funct. Mater.*, 2022, **32**, 2208962.

38 C. Han, S. Xiang, P. Xie, P. Dong, C. Shu, C. Zhang and J. X. Jiang, A universal strategy for boosting hydrogen evolution activity of polymer photocatalysts under visible light by inserting a narrow-band-gap spacer between donor and acceptor, *Adv. Funct. Mater.*, 2022, **32**, 2109423.

39 M. P. Murphy, H. Bayir, V. Belousov, C. J. Chang, K. J. Davies, M. J. Davies, T. P. Dick, T. Finkel, H. J. Forman, Y. Janssen-Heininger, D. Gems, V. E. Kagan, B. Kalyanaraman, N. Larsson, G. L. Milne, T. Nystrom, H. E. Poulsen, R. Radi, H. V. Remmen, P. T. Schumacker, P. J. Thornalley, S. Toyokuni, C. C. Winterbourn, H. Yin and B. Halliwell, Guidelines for measuring reactive oxygen species and oxidative damage in cells and in vivo, *Nat. Metab.*, 2022, **4**, 651–662.

40 S. Liu, B. Wang, Y. Yu, Y. Liu, Z. Zhuang, Z. Zhao, G. Feng, A. Qin and B. Z. Tang, Cationization-enhanced type I and type II ROS generation for photodynamic treatment of drug-resistant bacteria, *Angew. Chem., Int. Ed.*, 2022, **16**, 9130–9141.

41 H. Wu, L. Wang, Y. Wang, Y. Shao, G. Li, K. Shao and E. U. Akkaya, Targeted singlet oxygen delivery: a bioorthogonal metabolic shunt linking hypoxia to fast singlet oxygen release, *Angew. Chem., Int. Ed.*, 2022, **61**, e202210249.

42 S. Y. Lee, H. T. Do and J. H. Kim, Microplasma-assisted synthesis of TiO_2–Au hybrid nanoparticles and their photocatalytic mechanism for degradation of methylene blue dye under ultraviolet and visible light irradiation, *Appl. Surf. Sci.*, 2022, **573**, 151383.

43 Y. Li, D. Zhang, Y. Yu, L. Zhang, L. Li, L. Shi, G. Feng and B. Z. Tang, A cascade strategy boosting hydroxyl radical generation with aggregation-induced emission photosensitizers-albumin complex for photodynamic therapy, *Angew. Chem., Int. Ed.*, 2023, **17**, 16993–17003.

44 Y. Zou, Y. Zhang, Q. Yu and H. Chen, Dual-function antibacterial surfaces to resist and kill bacteria: Painting a picture with two brushes simultaneously, *J. Mater. Sci. Technol.*, 2021, **70**, 24–38.

45 B. Liu, F. Jiang, J. Sun, F. Wang and K. Liu, Biomacromolecule-based photo-thermal agents for tumor treatment, *J. Mater. Chem. B*, 2021, **9**, 7007–7022.

46 H. C. Flemming, E. D. Hullebusch, T. R. Neu, P. Nielsen, T. Seviour, P. Stoodley, J. Wingender and S. Wuertz, The biofilm matrix: multitasking in a shared space, *Nat. Rev. Microbiol.*, 2023, **21**, 70–86.

47 Y. Liu, L. Shi, L. Su, H. C. van der Mei, P. C. Jutte, Y. Ren and H. J. Busscher, Nanotechnology-based antimicrobials and delivery systems for biofilm-infection control, *Chem. Soc. Rev.*, 2019, **48**, 428–446.

48 J. Zhen, M. Zhao, Y. Ge, Y. Liu, L. Xu, C. Chen, Y. Gong and K. Yang, Construction, mechanism, and antibacterial resistance insight into polypeptide-based nanoparticles, *Biomater. Sci.*, 2019, **7**, 4142.

49 K. Lingaraju, R. B. Basavaraj, K. Jayanna, S. Bhavana, S. Devaraja, H. M. Kumar Swamy, G. Nagaraju, H. Nagabhushana and H. Raja Naika, Biocompatible fabrication of TiO_2 nanoparticles: Antimicrobial, anticoagulant, antiplatelet, direct hemolytic and cytotoxicity properties, *Inorg. Chem. Commun.*, 2021, **127**, 1387–7003.

50 C. Miao, L. Chu, D. Guo, X. Ding, W. Guo, S. Wang, J. Sheng, J. Zhang, Z. Wang and B. Zhou, Ferrocene-based porous polymer as advanced environmental remediation material for self-enhanced synergetic photothermal-enzymatic antibacterial and reversible iodine capture, *J. Environ. Chem. Eng.*, 2023, **11**, 110514.

51 T. Popescu, A. R. Lupu, V. Raditoiu, V. Purcar and V. S. Teodorescu, On the photocatalytic reduction of MTT tetrazolium salt on the surface of TiO_2 nanoparticles: Formazan production kinetics and mechanism, *J. Colloid Interface Sci.*, 2015, **457**, 108–120.

52 K. Ovchinnikov, C. Kranjec, T. Thorstensen, H. Carlsen and D. Diep, Successful development of bacteriocins into therapeutic formulation for treatment of MRSA skin infection in a murine model, *Antimicrob. Agents Chemother.*, 2020, **64**, 12.

53 Y. Liu, K. Yang, Y. Jia, J. Shi, Z. Tong, D. Fang, B. Yang, C. Su, R. Li, X. Xiao and Z. Wang, Gut microbiome alterations in high-fat-diet-fed mice are associated with antibiotic tolerance, *Nat. Microbiol.*, 2021, **6**, 874–884.

54 Y. Xi, J. Ge, M. Wang, M. Chen, W. Niu, W. Cheng, Y. Xue, C. Lin and B. Lei, Bioactive Anti-inflammatory, Antibacterial, Antioxidative Silicon-Based Nanofibrous Dressing Enables Cutaneous Tumor Photothermo-Chemo Therapy and Infection-Induced Wound Healing, *ACS Nano*, 2020, **14**, 2904–2916.

55 P. Tan, H. Fu and X. Ma, Design, optimization, and nanotechnology of antimicrobial peptides: From exploration to applications, *Nano Today*, 2021, **39**, 101229.